Zr-based metallic glasses Hugoniot under laser shock compression and spall strength evolution with the strain rate $>10^7$ s^{-1})

Yoann Raffray, Benjamin Jodar, Jean-Christophe Sangleboeuf, Alessandra Benuzzi-Mounaix, Tommaso Vinci, Laurent Berthe, Emilien Lescoute, Étienne Barraud, Erik Brambrink, Rémi Daudin, et al.

Contents lists available at ScienceDirect

International Journal of Impact Engineering

journal homepage: www.elsevier.com/locate/ijimpeng

Zr-based metallic glasses Hugoniot under laser shock compression and spall strength evolution with the strain rate (> 10^7 s^{-1})

Yoann Raffray [a], Benjamin Jodar [b,c], Jean-Christophe Sangleboeuf [a], Alessandra Benuzzi-Mounaix [d], Tommaso Vinci [d], Laurent Berthe [e], Emilien Lescoute [f], Etienne Barraud [b], Erik Brambrink [g], Rémi Daudin [h], Jean-Jacques Blandin [h], Didier Loison [a,*]

[a] Institute of Physics Rennes, UMR CNRS 6251, Rennes, France
[b] CEA, DAM, DIF, F-91297 Arpajon, France
[c] Université Paris Saclay, CEA, LMCE, F-91680 Bruyères-Le-Châtel, France
[d] LULI, CNRS, CEA, Sorbonne Université, École Polytechnique, Institut Polytechnique de Paris, F-91128 Palaiseau, France
[e] PIMM, UMR CNRS 8006, Paris, France
[f] CEA, DAM, CESTA, F-33114 Le Barp, France
[g] European XFEL, Holzkoppel 4, 22869, Schenefeld, Germany
[h] SIMaP, CNRS, University of Grenoble Alpes, 38000, Grenoble, France

ARTICLEINFO

Keywords:
Metallic glass
Laser shock compression
Hugoniot
Strain rate sensitivity
Spalling

ABSTRACT

We investigate the mechanical response of $Zr_{50}Cu_{40}Al_{10}$ and $Zr_{60}Cu_{30}Al_{10}$ metallic glasses under laser shock compression to reproduce hypervelocity impact conditions such as high longitudinal stresses and high strain rates in an unknown range of 10^6 — 10^7 s^{-1} . Hugoniot curves and strength parameters (spall strength and strain rate) are obtained from free surface velocity profiles and compared with previous studies on the mechanical behaviour of Zr-based metallic glasses under plate impact experiments. We established Hugoniot curves for both compositions up to 100 GPa, corresponding to a particle velocity of 1.8 km/s, and consistent with literature up to 75 GPa. Concerning the strength parameters, we studied the evolution of the spall strength with the strain rate and obtained data unreached up to now from 1.7×10^6 s^{-1} to 2.7×10^7 s^{-1}. This range of data correspond to strain rates of hypervelocity impacts of small debris (≈ 0.1 — 1 mm) on space infrastructure shields. Moreover, we highlight a strong dependency of the spall strength with the strain rate starting from 2×10^6 s^{-1}. Indeed, the spall strength increases from 2.6 GPa, close to its quasi-static tensile strength value, up to 13.6 GPa.

1. Introduction

Metallic Glasses also known as Amorphous Metallic Alloys have been of important interest over the last decades due to their astonishing mechanical properties in quasi-static conditions, generally superior to their crystalline counterpart (higher yield strength, lower density, higher tenacity and higher fracture threshold). As for their dynamic response, several studies [1–5], from 2011 to 2015, revealed the potential of metallic glasses as shielding components to improve the current space infrastructure shields. Li *et al.* [6] reported a large number of metallic glass compositions: ~ 10^3 discovered, ~ 10^5 considered and ~ 10^6 potential bulk metallic glass compositions. Some are more spread than others not only due to their mechanical properties, but also because they are much easier to synthetize with a better glass forming ability.

Regarding the suitability of Zr-based metallic glasses for mitigating hypervelocity impacts, many studies on the mechanical behaviour of Zr-based bulk metallic glasses under shock compression experiments have been published in the last twenty years [7–20] In most of these studies, authors collected Hugoniot data on their compositions of interest, calculated the Hugoniot Elastic Limit (σ_{HEL}) and studied the fracture mechanisms according to velocity profiles and post-mortem analysis at a strain rate up to 4.7×10^5 s^{-1}. It is important to note that in all of these publications, experimental data refer to shocked states induced by plate impact experiments. However, in the perspective of space debris mitigation, generating high strain rates, data reported up to now are not sufficient. Indeed, one can estimate the strain rate in the target considering the material of space debris, its size and its velocity using the equation from [11]:

* Corresponding author at: Glass mechanics department, IPR, UMR 6251, University of Rennes, Campus Beaulieu, 35042 Rennes Cedex, France.
E-mail address: didier.loison@univ-rennes.fr (D. Loison).

https://doi.org/10.1016/j.ijimpeng.2023.104755
Received 23 March 2023; Received in revised form 17 July 2023; Accepted 7 August 2023
Available online 9 August 2023

$$\varepsilon = \frac{u_t}{\delta_f}$$

With u_t the particle velocity in the target and δ_f the thickness of the flyer. To get the particle velocity in the target knowing the velocity of the debris, we used the polar shock method with the longitudinal stress versus particle velocity diagram reported by Martin *et al.* [7] on $Zr_{57}Nb_5Cu_{15.4}Ni_{12.6}Al_{10}$ (up to 120 GPa) and Xi *et al.* [9] on $Zr_{51}Ti_5Ni_{10}Cu_{25}Al_9$ (up to 110 GPa). Therefore, an aluminum debris at 7 km/s with a thickness from 3 mm to 0.1 mm would generate, in the Zr-based metallic glass target, strain rates from $9 \times 10^5\ s^{-1}$ to $2.7 \times 10^7\ s^{-1}$. Considering faster debris, more representative of actual space debris velocity, means that we would necessarily need to extrapolate the longitudinal stress versus particle velocity curve to apply the polar shock method.

In the present paper, we study the mechanical response under laser shock compression of two ternary ZrCuAl bulk and ribbon metallic glasses with very close compositions: $Zr_{50}Cu_{40}Al_{10}$ (rod and ribbon) and $Zr_{60}Cu_{30}Al_{10}$ (only rod). The main goal of this work is to better understand the mechanical response of these compositions under extreme conditions: high strain rates (10^6 - $10^7\ s^{-1}$) reachable thanks to laser shock experiments and corresponding to hypervelocity impacts of sub-millimeter debris, and high longitudinal stresses to investigate the potential of our compositions as shielding components of space infrastructures.

2. Experimental setup

2.1. Material properties

As mentioned in the introduction, we focus here on ternary bulk metallic glasses ($Zr_{50}Cu_{40}Al_{10}$ and $Zr_{60}Cu_{30}Al_{10}$) and ribbon metallic glasses ($Zr_{50}Cu_{40}Al_{10}$).

Rod metallic glasses have been synthetized by the Institute of Material Research (IMR) in Tohoku's University (Japan) [21], and in SIMaP laboratory (see Fig. 1-left) in Grenoble (France). Single master ingots of ternary $Zr_{50}Cu_{40}Al_{10}$ and $Zr_{60}Cu_{30}Al_{10}$ bulk metallic glasses were prepared by arc-melting mixtures of high purity zirconium, copper and aluminum under an argon atmosphere. The zirconium crystal rod used here contains an oxygen concentration less than 0.05 atomic percent to avoid crystallization during casting process. Master ingots were casted using the tilt-casting method for the IMR, to reduce the formation of cold shuts that act as crack-initiation sites (Yokoyama *et al.* [22]) and the succion casting method for the SIMaP, into millimetric diameter rods (from 5 mm to 10 mm).

Ribbons metallic glasses ($Zr_{50}Cu_{40}Al_{10}$), from SIMaP laboratory, were synthetized with a completely different process (see Fig. 1-right), called the melt-spinning method explained in details elsewhere [23]. Here the mixture is meticulously dropped on a high-speed copper wheel (2000 rpm). The high velocity of the wheel projects the ribbons into a big cylindrical reservoir long enough to cool down the metallic glass. The quench rate is strongly dependent on the wheel velocity. This method leads to approximately 5 mm wide and 40 μm thick ribbons.

For both ribbons and rod samples, the structure was characterized by X-ray diffractometry using Cu $K\alpha$ radiations on a Panalytical Empirean Diffractometer exhibiting no Bragg peak of any crystalline phase. The working conditions were: 40 kV and 40 mA for the X-ray tube, a scanning rate of 0.026° per step and recording in the 2θ range 20°–80° Glass-transition temperature T_g, crystallization temperature T_x and melting temperature T_m have been measured by differential-scanning calorimetry (DSC) at a heating rate of 20 K/min under nitrogen atmosphere (flow rate of 140 mL/min, to inhibit as much as possible oxidation of the sample) and using an amorphous silica pan. The initial density ρ_0 of our metallic glass compositions have been measured by Archimedes method with purified water. The other mechanical properties such as longitudinal sound speed C_L, transversal sound speed C_T, bulk sound speed C_b, Young's modulus, shear modulus and Poisson's ratio have been obtained using ultrasonic echography technique. Data are reported in Table 1.

Targets preparation for laser shock experiments consists in slicing up the original rods and polishing each piece up until the final thickness is reached ($\approx$70 μm). The polishing part has to be meticulously realised to make both faces of each sample parallels. As for the ribbons, no preparation is needed since it has originally a global thickness of approximately 40 μm.

2.2. Laser shock experiments

2.2.1. Laser facilities and in-situ diagnostics

Laser shock experiments have been performed on three different laser facilities: on the nano2000 and HERA facilities from the Laboratoire pour l'Utilisation des Lasers Intenses (LULI, UMR 7605, Institut Polytechnique de Paris, Palaiseau, France) and on the GCLT facility at CEA DAM DIF. Hereafter are listed the features of those laser facilities for shock configuration on metallic glass samples from 50 to 500 μm-thick. For each experimental campaigns, a high-power laser pulse at a wavelength of 1.053 μm is focused onto a target with a random phase

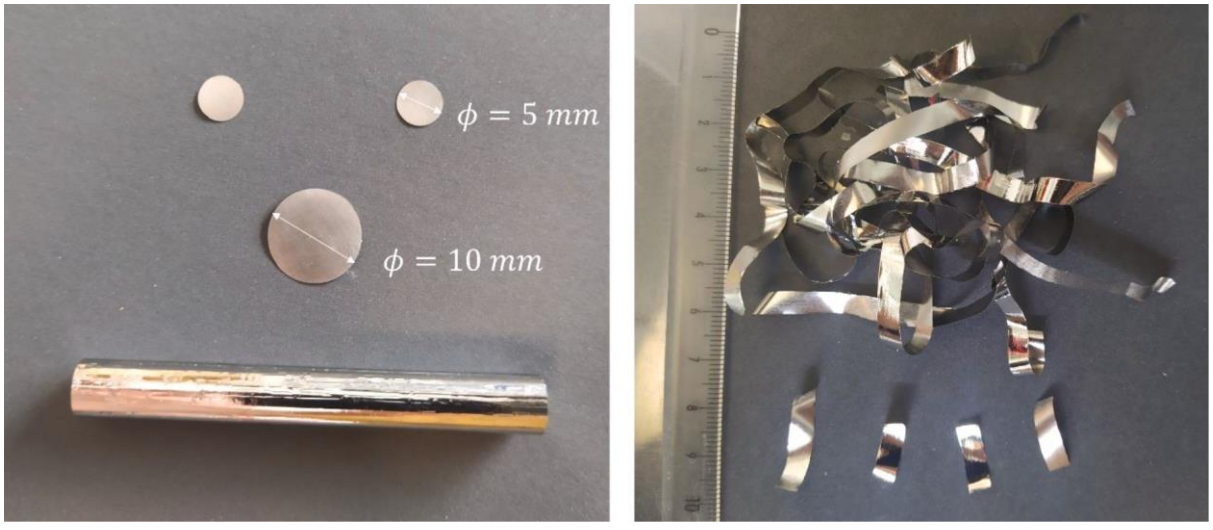

Fig. 1. Metallic glasses synthetized into rod shape (left) and ribbon shape (right).

Table 1
Mechanical properties and characteristic temperatures of $Zr_{50}Cu_{40}Al_{10}$ and $Zr_{60}Cu_{30}Al_{10}$metallic glasses studied in the present work synthetized by the Institute of Material Research (IMR) and SIMaP laboratory. With ρ_0, C_L, C_T , C_b, E, G, ν, T_g , T_x and T_m respectively the density, the longitudinal and the transversal sound speed, the bulk sound speed, the Young modulus, the shear modulus, the Poisson's ratio, the glass transition temperature, the crystallization temperature and the melting temperature.

	$Zr_{60}Cu_{30}Al_{10}^{IMR}$	$Zr_{50}Cu_{40}Al_{10}^{IMR}$	$Zr_{50}Cu_{40}Al_{10}^{SIMaP-Rod}$	$Zr_{50}Cu_{40}Al_{10}^{SIMAP-Ribbon}$
ρ_0 [g..cm^{-3}]	6.703 ± 0.003	6.854 ± 0.005	6.909 ± 0.011	7.140 ± 0.171
C_L [km..s^{-1}]	4.76 ± 0.04	4.81 ± 0.04	4.82 ± 0.02	–
C_T [km·s^{-1}]	2.126 ± 0.015	2.188 ± 0.015	2.205 ± 0.002	–
C_b [km..s^{-1}]	4.080 ± 0.055	4.091 ± 0.056	4.094 ± 0.002	–
E [GPa]	81.9 ± 2	89.3 ± 2	91.9 ± 1	–
G [GPa]	29.8 ± 2	32.7 ± 2	33.6 ± 1	–
ν	0.375 ± 0.002	0.365 ± 0.002	0.368 ± 0.008	–
T_g [°C]	383 ± 5	422 ± 5	427 ± 5	421 ± 5
T_x [°C]	470 ± 5	507 ± 5	505 ± 5	505 ± 5
T_m [°C]	–	786 ± 5	779 ± 5	793 ± 5

plate and a lens to ensure a uniform spatial energy distribution. In order to avoid laser breakdown in air (which would strongly reduce the laser energy deposit on the front surface of the sample) the experimental setup is placed in a vacuum chamber (10^{-3} mbar).

Laser shock experiments on several laser facilities not only give the opportunity to collect data on different pressure ranges, but also to check the consistency and the reproducibility of the results by comparing the data collected on two different laser facilities at a same pressure range. Considering the laser shot configurations specified in Table 2, some longitudinal stress ranges are reachable on different laser facilities (from 15 to 100 GPa for nano2000, 7 to 30 GPa for HERA and 6 to 23 GPa for GCLT).

To record the free surface velocity profile and collect Hugoniot data, two types of VISAR (Velocity Interferometer System for Any Reflector) have been used. First, a point VISAR [24] (Fig. 2-a) with a continuous 532 nm laser beam (Verdi), used on HERA and GCLT facilities. To reduce the temperature rise imparted by the laser probe and therefore reduce the risk to reach the glass-transition temperature leading to potential crystallization or even melting, we added a thin layer of silver (≈ 100 nm) on the rear surface to improve the sample reflectivity and reduce the laser probe power (ϕ_{foc} = 50 μm and P_{Verdi} = 0.3 W). Secondly, a line-imaging velocimeter [25] (Fig. 2-b), used on nano2000 facility allows to record the free surface velocity on a line of approximately 0.9 mm long in our case. The line-imaging velocimeter system is basically a dual interferometer system: one with a pulsed laser beam of 1064 nm (ω) and a sensitivity S_1 (in km..s^{-1}..fringe^{-1}) and the second with a pulsed laser beam of 532 nm (2ω) and a sensitivity S_2 (with $S_1 \neq S_2$ to resolve fringes ambiguities). Since the line-imaging velocimeter uses pulsed laser beams, there is no important heating due to the probe laser during the experiment. Adding a thin layer of silver in this situation is therefore not needed. Readers must refer to Fig. 3-a) to see how a streak image from line-imaging velocimeter looks like. The fringe shift, indicated with white arrows, represents the shock front breakout. From this image, one can clearly notify the flatness of the shock front and that the energy distribution is uniform. The brightness of the fringes means that the reflectivity is sufficient to deduce a velocity profile (cf Fig. 3-b). Note that every shot using line visar were post-processed with Neutrino (software developed by Tommaso Vinci [26]).

Table 2
Laser facilities features for shock experimentations conducted with E, τ, ϕ_{foc}, σ_L and $\dot{\varepsilon}$ respectively the laser energy, the pulse duration, the diameter of the focal spot, the longitudinal stress and the strain rate (σ_L and $\dot{\varepsilon}$ extracted from measurements).

Laser facility	E (J)	τ (ns)	ϕ_{foc} (mm)	Intensity (TW/cm^2)	σ_L (GPa)	$\dot{\varepsilon}$ ($10^7 s^{-1}$)
nano2000	100 - 800	10 and 15	0.9 and 1.7	1.1 – 10	15 – 100	0.64 – 2.7
HERA	20 - 200	15	1.07	0.1 – 1.4	7 – 30	0.17 – 0.83
GCLT	10 - 50	10 and 15	1	0.1 – 0.65	6 – 23	–

2.2.2. Method

Once the velocity profile is obtained (Fig. 3-b), the shock velocity U_s can be calculated through:

$$U_s = \frac{\text{sample thickness}}{t_{shock}} \quad (1)$$

With t_{shock} the time at which the shock front reaches the rear surface. The time reference ($t = 0$) corresponds to the laser impact on the target. Therefore, t_{shock} includes the laser-matter interaction and the time it takes to the compression waves to turn into a shock wave and to travel through the sample. The steeper the loading temporal profile is, the quicker the pressure increase is, and consequently, the shorter the time to the compression waves to turn into a shock wave is. The loading temporal profile was steep enough during our experiments to use this equation without generating significant discrepancies. Then, to derive the particle velocity from the free surface velocity profile we assume that the Hugoniot and isentropic curves are superimposed in the longitudinal stress versus particle velocity diagram. Considering this assumption, usually mentioned as the free surface approximation for a weak shock, the free surface velocity is on average twice the particle velocity [27]:

$$U_p \approx \frac{U_{fs}}{2} \quad (2)$$

Considering now the Rankine-Hugoniot relationships, we calculate the longitudinal stress and the density after the shock compression:

$$\sigma_L - \sigma_{L0} = \rho_0 \left(U_s - U_{p0}\right)\left(U_p - U_{p0}\right) \quad (3)$$

$$\rho = \rho_0 \frac{U_s - U_{p0}}{U_s - U_p} \quad (4)$$

With ρ_0 the initial density, $U_{p0} = 0$ the initial particle velocity and $\sigma_{L0} = 0$ (sample initially at rest). Rankine-Hugoniot relationships become:

$$\sigma_L = \rho_0 U_p U_s \quad (5)$$

$$\rho_1 = \rho_0 \frac{U_s}{U_s - U_p} \quad (6)$$

Then, from the velocity profile in Fig. 4 characteristic of spallation, with the oscillations resulting from the reflections of the compression and release waves inside the spall, the spall strength σ_R and the strain rate $\dot{\varepsilon}$ can be calculated. For the strain rate, we applied the well-used equation:

$$\dot{\varepsilon} = -\frac{1}{2C_b}\frac{\Delta U_{fs}}{\Delta t} \quad (7)$$

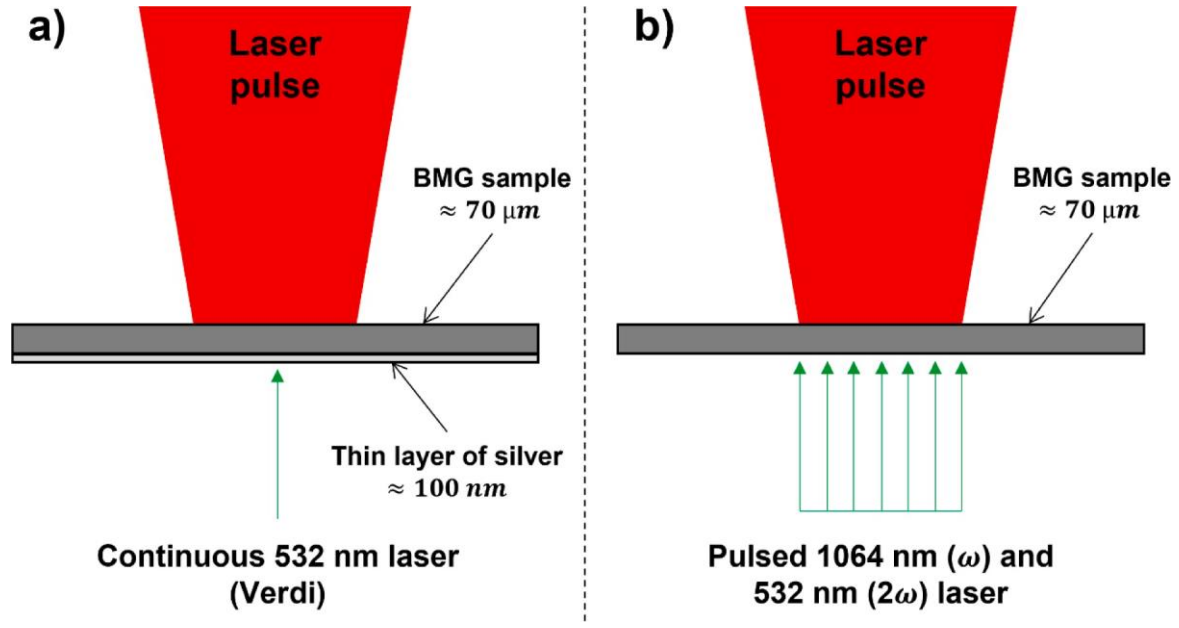

Fig. 2. Experimental setup with (a) point VISAR used on HERA and GCLT facilities (the layer of silver was only on GCLT facility) and (b) a line-imaging velocimeter used on nano2000 facility.

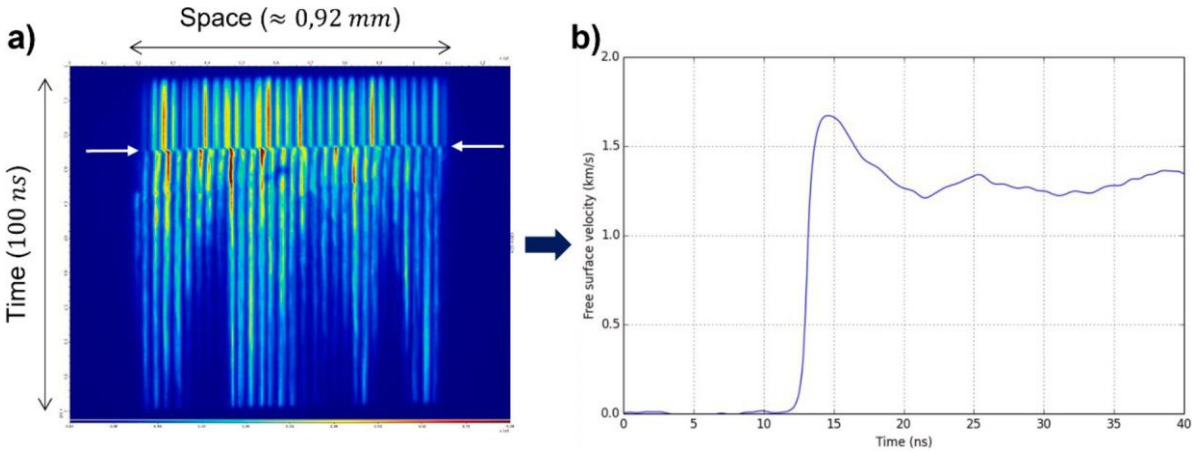

Fig. 3. Streak image from line imaging velocimeter (a) (white arrows correspond to front shock breakout at the rear surface) and the associated velocity profile of the free surface (b) post-processed with Neutrino.

With C_b the sound bulk velocity, $\Delta U_{fs} = U_{max} - U_{min}$ where U_{max} is the free surface velocity after the shock breakout and U_{min} the first minimum on the velocity profile corresponding to pullback velocity. At last, Δt is the time difference between U_{min} and U_{max} : $\Delta t = t(U_{max}) - t(U_{min})$. With this equation, we calculate the average strain rate between U_{min} and U_{max} related to the increased tensile stress in the target.

As for the spall strength, three main equations have been used in previous studies:

- The Novikov equation [28]:

$$\sigma_{spall} = \frac{1}{2}\rho_0 C_b \Delta U_{fs} \quad (8)$$

using the acoustic approximation (used in [29–34])

- A variant of the Novikov equation when dealing with elastic shock waves:

$$\sigma_{spall} = \frac{1}{2}\rho_0 C_L \Delta U_{fs} \quad (9)$$

with C_L the longitudinal sound speed (used in [10,11,13,15,16])

- And the Stepanov equation [28]:

$$\sigma_{spall} = \rho_0 C_b \Delta U_{fs} \frac{C_L}{C_L + C_b} \quad (10)$$

taking into account the elasto-plastic behaviour of the material (used in [18–20,35]). For our metallic glass compositions, the spall strength calculated with the Stepanov equation is approximately 8 % higher than the one calculated with Novikov equation. This relative shift is constant for a given metallic glass composition. It only depends on the material properties ρ_0, C_L and C_T.

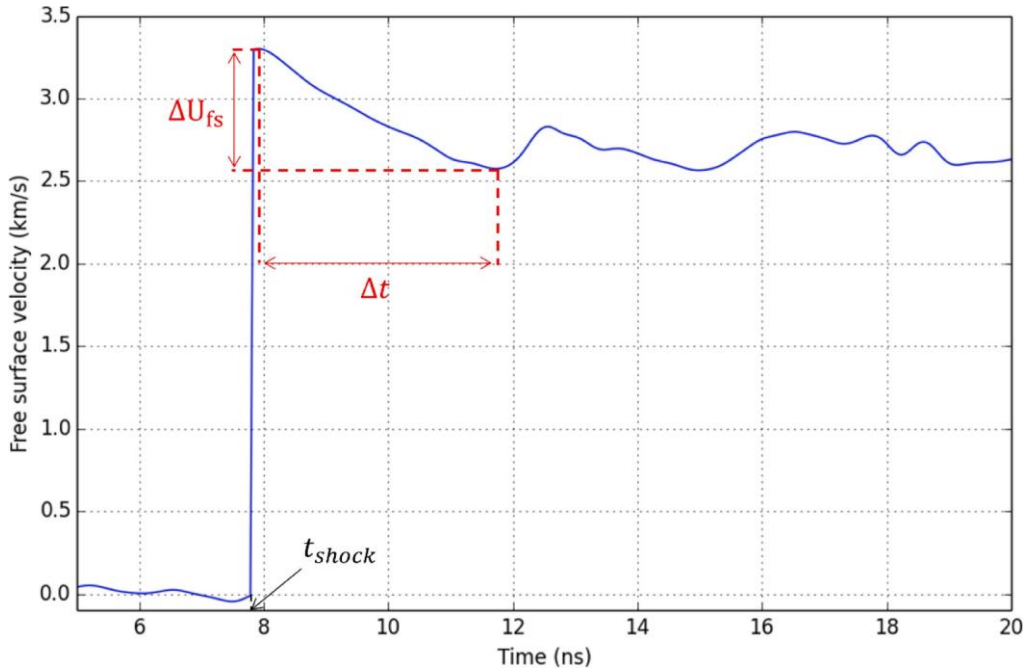

Fig. 4. Typical free surface velocity profile with oscillations indicative of spallation. Laser shot performed on a 64 μm thick Zr_{60} Cu_{30} Al_{10} sample with a laser pulse energy of 552 J and an impulsion time of 15 ns focus on a 0.9 mm diameter spot leading to an intensity of 5.9 TW/cm².

In this work, we decided to use the Stepanov equation which takes into account the mechanical behaviour of the sample. In the following part, we compare our results with those from literature obtained on Zr-based bulk metallic glasses and on other classical metals such as aluminum and copper. To ensure consistency when comparing all studies, spall strength and strain rate values from literature have been corrected according to Stepanov method using available velocity profiles and respective mechanical properties.

3. Results and discussion

3.1. Hugoniot states

Readers will find on Fig. 5 nine free surface velocity profiles of $Zr_{50}Cu_{40}Al_{10}$ metallic glass samples, with thicknesses between 64 μm and 77 μm, under laser shock compression performed on GCLT (shots 1 and 2), HERA (shots 3—5) and nano2000 (shots 6–9) to cover a wide range of particle velocities (from 190 to 1720 m/s) and, therefore, longitudinal stresses (from 7 to 74 GPa). Corresponding Hugoniot data such as the particle velocity U_p, the shock wave velocity U_s, the longitudinal stress σ_L and the density ρ are reported in Table 3. All nine shots

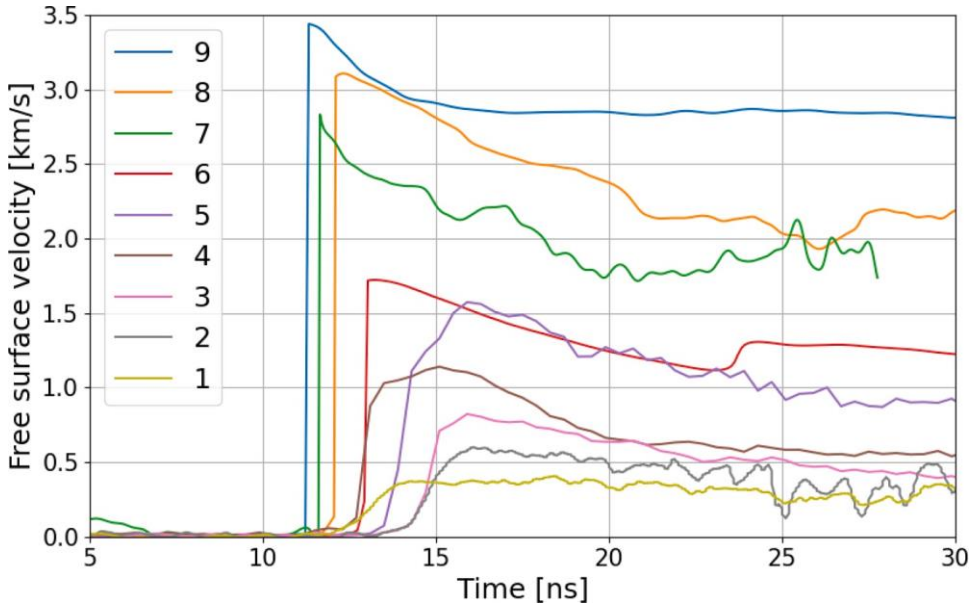

Fig. 5. Free surface velocity profiles of $Zr_{50}Cu_{40}Al_{10}$ metallic glass samples (from IMR) under laser shock compression performed on GCLT, HERA and nano2000 facilities.

Table 3
Hugoniot data calculated from the free surface velocity profiles of Fig. 5. U_p, U_s, σ_L and ρ are respectively the particle velocity, the shock wave velocity, the longitudinal stress and the density calculated with Eqs. (1–6).

Shot	Sample thickness [μm]	U_p [km/s]	U_s [km/s]	σ_L [GPa]	ρ [g/cm^3]
1	69.5 ± 2	0.186 ± 0.019	5.28 ± 0.28	6.7 ± 0.8	7.1 ± 0.6
2	75 ± 2	0.300 ± 0.030	5.14 ± 0.25	10.6 ± 1.2	7.3 ± 0.6
3	77 ± 2	0.412 ± 0.041	5.31 ± 0.26	15.0 ± 1.7	7.4 ± 0.6
4	69 ± 2	0.571 ± 0.057	5.42 ± 0.30	21.2 ± 2.4	7.7 ± 0.7
5	74.5 ± 2	0.787 ± 0.079	5.46 ± 0.28	29.4 ± 3.3	8.0 ± 0.7
6	75 ± 2	0.862 ± 0.060	5.93 ± 0.29	35.0 ± 2.8	8.0 ± 0.7
7	64 ± 1	1.420 ± 0.140	5.52 ± 0.33	53.6 ± 6.2	9.2 ± 1.2
8	69 ± 2	1.555 ± 0.100	5.81 ± 0.25	61.9 ± 4.9	9.4 ± 0.9
9	70 ± 2	1.720 ± 0.080	6.24 ± 0.32	73.6 ± 5.2	9.5 ± 1.0

have been performed on $Zr_{50}Cu_{40}Al_{10}$ metallic glass samples synthetized by the IMR. Readers will find its material properties in Table 1.

Hugoniot curves, representing the longitudinal stress and the shock wave velocity versus the particle velocity are established and discussed in Fig. 6. We are now able to compare not only $Zr_{50}Cu_{40}Al_{10}$ and $Zr_{60}Cu_{30}Al_{10}$ metallic glasses but also the fabrication process on a unique composition (here $Zr_{50}Cu_{40}Al_{10}$). Listed hereafter are the main observations one can do on Fig. 6:

- Laser shock experiments on such metallic glasses led to longitudinal stresses up to 100 GPa with data well distributed all along the longitudinal stress versus particle velocity diagram (Fig. 6-a).
- One can distinguish 4 regions on the shock velocity versus particle velocity diagram (Fig. 6-b): $U_p \leq 0.17$ km/s, $0.17 \leq U_p \leq 0.5$ km/s, $0.5 \leq U_p \leq 1.55$ km/s and $U_p \geq 1.55$ km/s. As discussed later, these regions can be associated to an elasto-plastic behaviour (R_1 and R_2), a structural change (R_3)or eventually a change of state (R_4).
- As for the particle velocity uncertainties, depending on the diagnostic used, it is either proportional or estimated on a case-by-case basis. The first case concerns the point VISAR measurements. Considering the uncertainties on the fringe shift, on the interfringe determination and the velocity sensitivity of the VISAR, we end up with a 10 % uncertainty on the particle velocity. It concerns the quasi totality of data between 6 and 30 GPa. The second case, concerning the line imaging velocimeter, starts with the same sources of uncertainties but with a much lower velocity sensitivity. We add to those uncertainties, the ones coming from the post-processing software Neutrino on the phase of the signal, which can really differ from one experiment to another, depending on the rear surface reflectivity for example. This finally leads to uncertainties on the particle velocity from 4.6 % up to 15 %.
- Therefore, on the first order, the compound ratio in the ZrCuAl system and the fabrication process of these metallic glasses do not significantly affect the mechanical response under laser shock experiments.

From now on, we gather all results on $Zr_{50}Cu_{40}Al_{10}$ regardless the fabrication process for the sake of clarity. However, we still consider $Zr_{50}Cu_{40}Al_{10}$ and $Zr_{60}Cu_{30}Al_{10}$ compositions separately.

To go further in the analysis of the experimental data shown in Fig. 6, we now compare with previous works on Zr-based bulk metallic glasses: Martin *et al.* [7] on $Zr_{57}Nb_5Cu_{15.4}Ni_{12.6}Al_{10}$, Mashimo *et al.* [8] on $Zr_{55}Al_{10}Ni_5Cu_{30}$, Xi *et al.* [9] on $Zr_{51}Ti_5Ni_{10}Cu_{25}Al_9$, Smirnov *et al.* [10] on ZrCuAlNi and Li *et al.* [11] on $Zr_{70}Cu_{13}Ni_{9.8}Al_{3.6}Nb_{3.4}Y_{0.2}$. All data from literature have been obtained with plate impact experiments. Hereafter are the main observations on Fig. 7:

- Laser shock experiments led to much more dispersion than literature data with plate impact experiments. It is yet well-counterbalanced with the number of data one can obtain thanks to the higher shot rate of laser facilities (63 new data points in this paper).
- Different regions are also noticeable on the shock velocity versus particle velocity diagram. Indeed, Mashimo *et al.* [8] mentioned 3 regions: $U_p \leq 0.17$ km/s, $0.17 \leq U_p \leq 0.38$ km/s and $U_p \geq 0.38$ km/s with a maximum particle velocity at 1.25 km/s. As for Martin *et al.* [7], 4 regions are mentionned: $U_p \leq 0.24$ km/s, $0.27 \leq U_p \leq 0.72$ km/s, $0.72 \leq U_p \leq 1.71$ km/s and $U_p \geq 1.71$ km/s. In both papers, data from the first two regions (R_1 and R_2) result from velocity profiles with a two-waves structure indicative of an elastic-plastic response. Due to the low thicknesses of our samples ($\lesssim$ 70 μm), we did not observe any two-waves structure velocity profile. That is why the distinction between the elastic and the plastic regions cannot be done so easily like in [7] and [8]. Concerning the third region R_3, even if the particle velocity domain slightly differs from our data to [7] and [8], each study as well as our results display a plateau of the shock wave velocity with the particle velocity. The main difference between our results and data from literature is the evolution of the shock wave velocity in the fourth region R_4, starting at a particle velocity of 1.5 km/s, which is much steeper than in Martin *et al.* [7] and Li *et al.* [9] papers. This difference is also noticeable on Fig. 7-a) with a higher longitudinal stress than in literature for an equivalent particle velocity.
- Given the previous comments and the uncertainties, on the first order, the system of the Zr-based metallic glasses does not seem to affect the mechanical behaviour under shock compression. Data from this work are really close to those in the literature on the longitudinal stress versus particle velocity diagram up to 70 GPa and an equivalent particle velocity of 1.7 km/s which corresponds to the beginning of R_4. Laser shock experiment is therefore a well-adapted technique to establish the equation of state of our metallic glasses.

From now on, we may discuss the origin of such a difference in the fourth region R_4. A primary interpretation is to link this change of behaviour to the metallic glass composition. Indeed, a different composition system leads naturally to a different structure which could possibly change the mechanical response starting from a critical longitudinal stress. The higher the longitudinal stress, the more intense the divergence in mechanical response is, due to the localized plasticity (or even homogenized plasticity at this pressure level) which strongly depends on the structure. However, given that Martin *et al.* [7] and Xi *et al.* [9] obtained extremely close results on two different system up to 110 GPa, this dependence of the mechanical behaviour with the composition system would seem to be specific to our ternary metallic glasses ZrCuAl. Therefore, this change in the mechanical response starting around 75 GPa could find its origin elsewhere. Another possible assumption we develop here is based on a change of state. Firstly, the reflectivity of the rear surface was lost for some of the most intense shots on the streak images few nanoseconds after the shock wave arrival. We consequently suspect melting or at least partial melting during the release process. Secondly, this suspicion of melting is reinforced by Wen *et al.* [36] and Demaske *et al.* [37] research on $Zr_{50}Cu_{50}$ metallic glass under shock loading with molecular dynamic simulations. Indeed in these papers, Wen *et al.* [36] and Demaske *et al.* [37] plot the evolution of the flow stress which is exponentially decreasing with increasing longitudinal stress from $\sigma_L = 10$ GPa. This decrease is such that the flow stress τ_{flow} reaches 0 GPa for a longitudinal stress of 73 GPa and 65 GPa respectively. The flow stress decreasing towards 0 GPa means that the sample completely lose its ability to resist shear and, therefore, is not solid anymore.

Finally, we still do not have enough elements to justify with certainty this difference between our results and literature in R_4. However, if the assumption of a change of state turns out to be true, we could reconsider the application of the free surface approximation ($U_p = \frac{U_fs}{2}$) since the isentropic curve would be no more symmetrical to the Hugoniot curve in

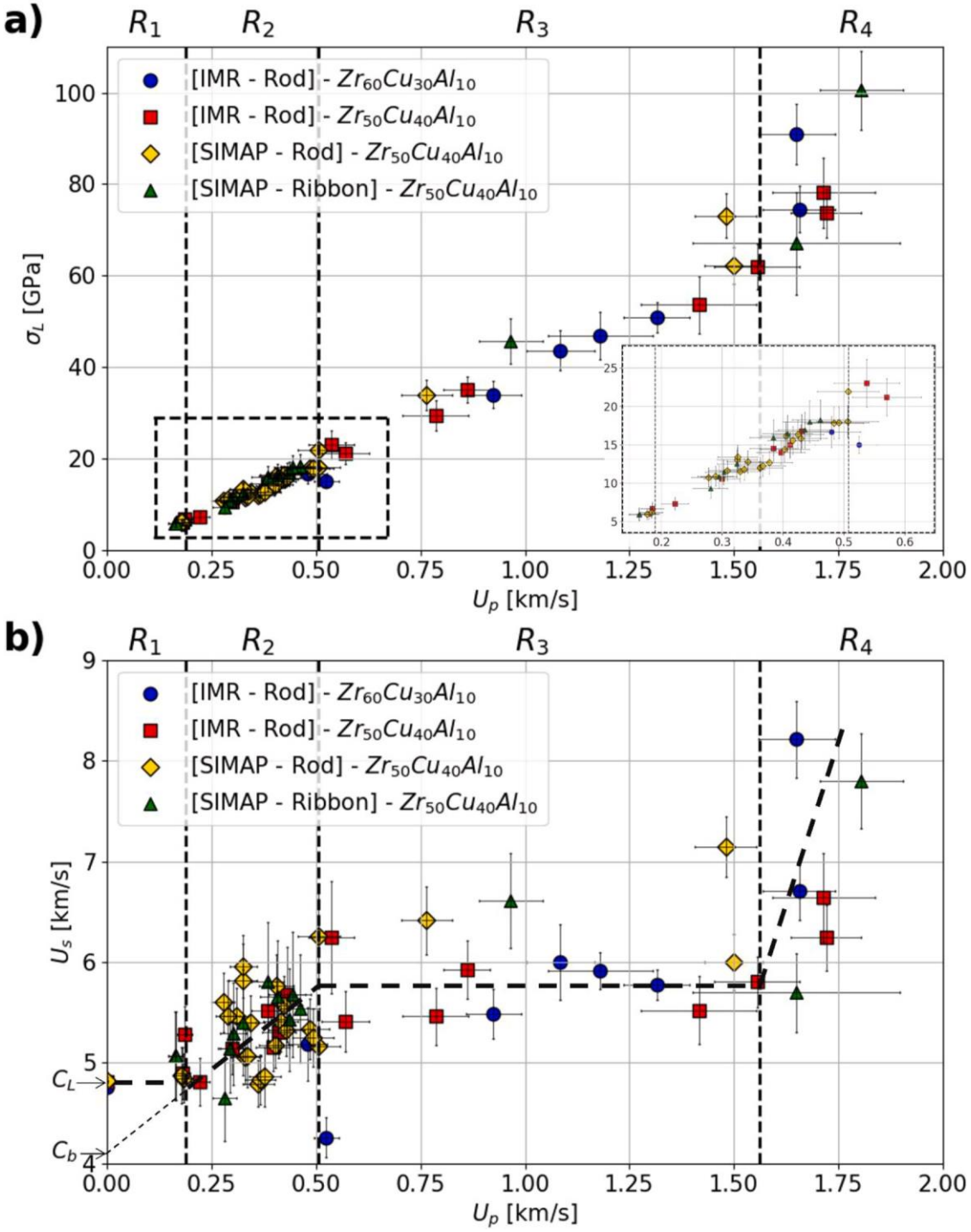

Fig. 6. Experimental Hugoniot curves of metallic glasses studied in this present work. Longitudinal stress versus particle velocity (a) and shock wave velocity versus particle velocity (b).

such a case. We may then underestimate the particle velocity and the longitudinal stress as a result.

3.2. Spall strength evolution with strain rate

Five free surface velocity profiles exhibiting spallation process with spall strengths between 6.8 GPa and 13.6 GPa, and strain rates between 7.5×10^6 s^{-1} and 2.6×10^7 s^{-1} are grouped together on Fig. 8. Spall strengths and strain rates, calculated from this velocity profiles are reported in Table 4. Here again, readers must refer to Table 1 to consider the proper material properties depending on the metallic glass sample considered.

Firstly, we investigate the influence of the longitudinal stress on the spall strength. Li *et al.* [38] research's on carbon mild steel demonstrated that the spall strength is strongly dependent on the peak stress and on the strain rate in ranges from 2 GPa to 10 GPa and from 0.4×10^5 s^{-1} to 8×10^5 s^{-1} respectively. Nevertheless, the spall strength seems to reach a plateau for peak stresses above 7 GPa. As for Zr-based metallic glasses, *Li et al.* [11] research's on $Zr_{70}Cu_{13}Ni_{9.8}Al_{3.6}Nb_{3.4}Y_{0.2}$ showed that the spall strength appears to be relatively constant around 2.3 GPa with the

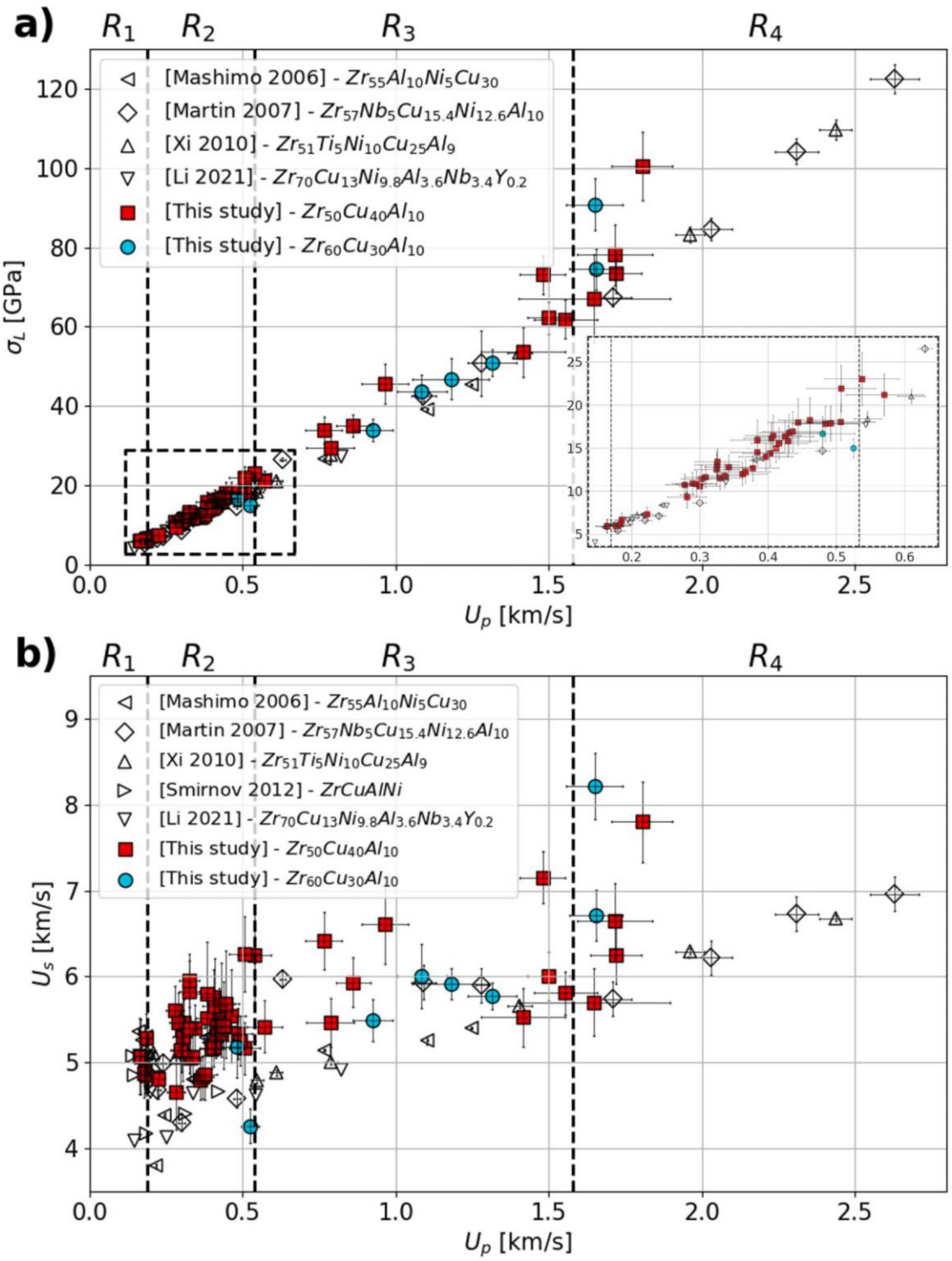

Fig. 7. Confrontation of experimental Hugoniot curves obtained in this work with literature on Zr-based metallic glasses. Longitudinal stress versus particle velocity (a) and shock wave velocity versus particle velocity (b).

longitudinal stress varying from 4 GPa to 27 GPa. From the Table 5, gathering our data from laser shock experimental campaigns on $Zr_{50}Cu_{40}Al_{10}$ and $Zr_{60}Cu_{30}Al_{10}$ metallic glasses (free surface velocities, longitudinal stresses, spall strengths and strain rates), one can extract five data pairs with an equivalent strain rate but different longitudinal stresses values. We then plot on Fig. 9 the spall strength as a function of longitudinal stress for each data pair corresponding to these five values of strain rate from $3.9 \times 10^6\ s^{-1}$ to $2.6 \times 10^7\ s^{-1}$. It turns out that the spall strength increases with the strain rate but is nevertheless independent of the longitudinal stress. From now on, we are interested in the evolution of the spall strength as a function of the strain rate.

On Fig. 10 are shown our results against literature data reported on Zr-based bulk metallic glasses subjected to plate impact experiments. The marker's shape refers to the main author while the color refers to the metallic glass composition. Related uncertainties in Table 5 appear large due to the uncertainties on the particle velocity which can reach the

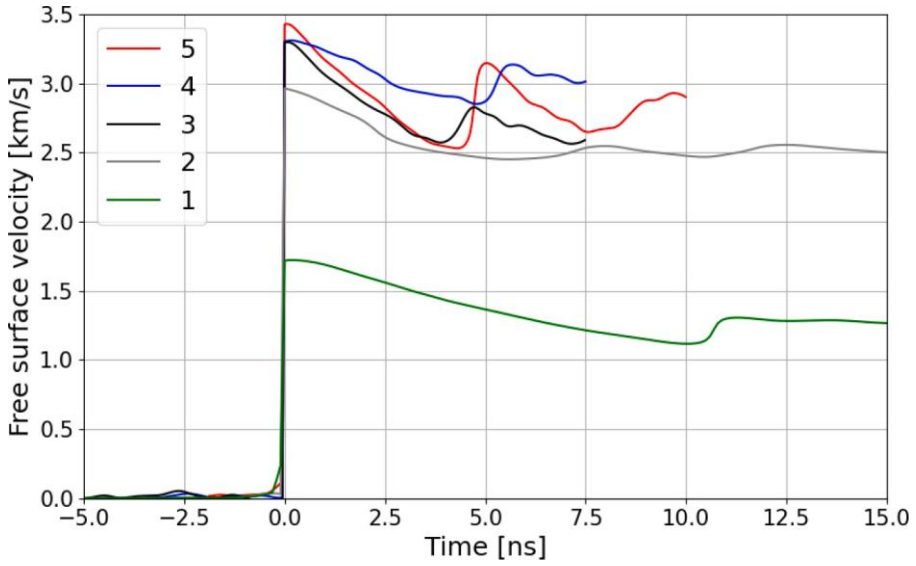

Fig. 8. Free surface velocity profiles exhibiting spalling process of $Zr_{60}Cu_{30}Al_{10}$ and $Zr_{50}Cu_{40}Al_{10}$ metallic glasses.

Table 4

Spall strengths and strain rates calculated from the velocity profiles of Fig. 8. Readers must refer to Table 1 to consider the proper material properties depending on the metallic glass sample.

Shot	Sample	σ_R [GPa]	$\dot{\varepsilon}$ [10^6 s^{-1}]
1	$Zr_{50}Cu_{40}Al_{10}^{IMR}$	9.2 ± 2.8	7.5 ± 2.3
2	$Zr_{50}Cu_{40}Al_{10}^{SIMaP—Rod}$	7.9 ± 4.1	11.3 ± 5.9
3	$Zr_{60}Cu_{30}Al_{10}^{IMR}$	10.7 ± 6.3	23.4 ± 13.8
4	$Zr_{60}Cu_{30}Al_{10}^{IMR}$	6.8 ± 5.7	12.2 ± 10.3
5	$Zr_{50}Cu_{40}Al_{10}^{IMR}$	13.6 ± 5.8	25.8 ± 11.1

Table 5

List of spall strengths and strain rates values on Zr_{60} Cu_{30} Al_{10} and Zr_{50} Cu_{40} Al_{10} bulk metallic glasses with the associated free surface velocities and longitudinal stresses.

Composition	U_{sl} [km /s]	σ_L [GPa]	$\dot{\varepsilon}$ [10^6 s^{-1}]	σ_R [GPa]
$Zr_{60}Cu_{30}Al_{10}$	3.31 ± 0.17	74.5 ± 5.1	12.2 ± 10.3	6.8 ± 5.7
	1.85 ± 0.13	34.0 ± 2.9	9.4 ± 4.3	9.2 ± 4.3
	2.63 ± 0.16	50.9 ± 3.3	22.8 ± 11.2	9.2 ± 4.5
	2.17 ± 0.16	43.7 ± 4.3	18.6 ± 10.6	9.4 ± 5.3
	3.30 ± 0.18	90.9 ± 6.6	23.2 ± 13.7	10.7 ± 6.3
	2.36 ± 0.25	46.8 ± 5.2	26.8 ± 11.6	13.0 ± 5.63
$Zr_{50}Cu_{40}Al_{10}$	0.37 ± 0.04	6.8 ± 0.7	2.0 ± 0.7	2.6 ± 0.9
	0.46 ± 0.05	8.3 ± 0.8	1.7 ± 0.7	2.8 ± 1.1
	0.45 ± 0.05	8.2 ± 0.8	2.0 ± 0.7	3.0 ± 1.1
	0.65 ± 0.07	13.1 ± 1.5	3.9 ± 1.2	5.1 ± 1.5
	1.27 ± 0.13	34.2 ± 5.4	3.9 ± 2.2	5.8 ± 3.3
	0.82 ± 0.08	15.0 ± 1.7	3.6 ± 0.7	6.3 ± 1.2
	1.53 ± 0.12	33.9 ± 3.2	6.4 ± 2.8	7.0 ± 3.1
	1.01 ± 0.10	21.9 ± 2.7	6.4 ± 2.3	7.1 ± 2.4
	3.0 ± 0.14	62.2 ± 4.1	8.3 ± 4.2	7.8 ± 3.9
	2.96 ± 0.15	73.1 ± 4.8	11.3 ± 5.9	7.8 ± 4.1
	1.14 ± 0.11	21.2 ± 2.4	7.9 ± 1.9	8.6 ± 1.9
	1.21 ± 0.12	17.6 ± 2.9	8.3 ± 2.6	9.2 ± 2.8
	1.2 ± 0.11	35.0 ± 2.8	7.5 ± 2.3	9.2 ± 2.8
	1.57 ± 0.16	29.4 ± 3.3	7.9 ± 2.1	10.6 ± 2.7
	3.1 ± 0.21	61.9 ± 4.9	20.2 ± 8.1	13.5 ± 5.4
	3.43 ± 0.25	78.1 ± 7.6	25.8 ± 11.1	13.6 ± 5.8

same order of magnitude than the difference velocity ΔU_{fs} between the free surface velocity after the shock wave breakout and the first minimum before the pullback. Spall strengths and strain rates presented here have been calculated for bulk metallic glass samples only. We do not have any results for ribbon metallic glasses since we do not know the bulk sound speed. Here again, we list the main observations one can do on Fig. 10:

- Laser driven shock compression induces higher strain rates compared to plate impact experiments. Reported strain rate values from plate impact experiments are between 6.2×10^4 s^{-1} and 4.7×10^5 s^{-1} while in this work, we have collected data from 1.7×10^6 s^{-1} up to 2.7×10^7 s^{-1}.
- The spall strength is increasing with the strain rate starting from 2×10^6 s^{-1} which was not revealed on bulk metallic glasses in the literature since plate impact experiments are limited to approximately 10^6 s^{-1}. Indeed, literature data are located around 3 ± 1 GPa while in this work, we report spall strength values up to 13.6 GPa, wich is actually almost 7 times higher than the tensile strength of 2 GPa in quasi-static experiments performed by Yokoyama *et al.* [21] on $Zr_{50}Cu_{40}Al_{10}$.
- As used by Cuq-Lelandais *et al.* in [32] and [39], a power law fit has been chosen to express the spall strength evolution with the strain rate. To better fit the quasi-static tensile strength of 2 GPa [21], we finally consider the relation:

$$\sigma_R\,[GPa] = 9.37 \times 10^{-4}\dot{\varepsilon}^{0.548} + \sigma_R^{QS} \quad (11)$$

With σ_R^{QS} = 2 GPa. This equation has been obtained with the experimental data from this work only ($Zr_{50}Cu_{40}Al_{10}$ and $Zr_{60}Cu_{30}Al_{10}$) - we then assume here that the tensile strength of $Zr_{60}Cu_{30}Al_{10}$ is close to 2 GPa given the uncertainties. Nevertheless, one can notice that the dashed line fits well the experimental data including the data from literature.

Such an evolution of the spall strength with the strain rate has already been observed on other materials such as aluminum ([29–33,35,40]) and copper ([29,30,34,35]). On Fig. 11, all data on Zr-based metallic glasses from this work (blue circles) and from literature (blue triangles) are group together and compared with data on aluminum (grey markers) and copper (orange markers). Here again, markers' shape refers to the main author. To remain consistent, we use a similar relationship than (Eq. (9)) to obtain the dash lines with aluminum and copper data. This time, since we do not know exactly the type of aluminum and copper used in these studies, we let the constant as a free parameter. We then get the following relations:

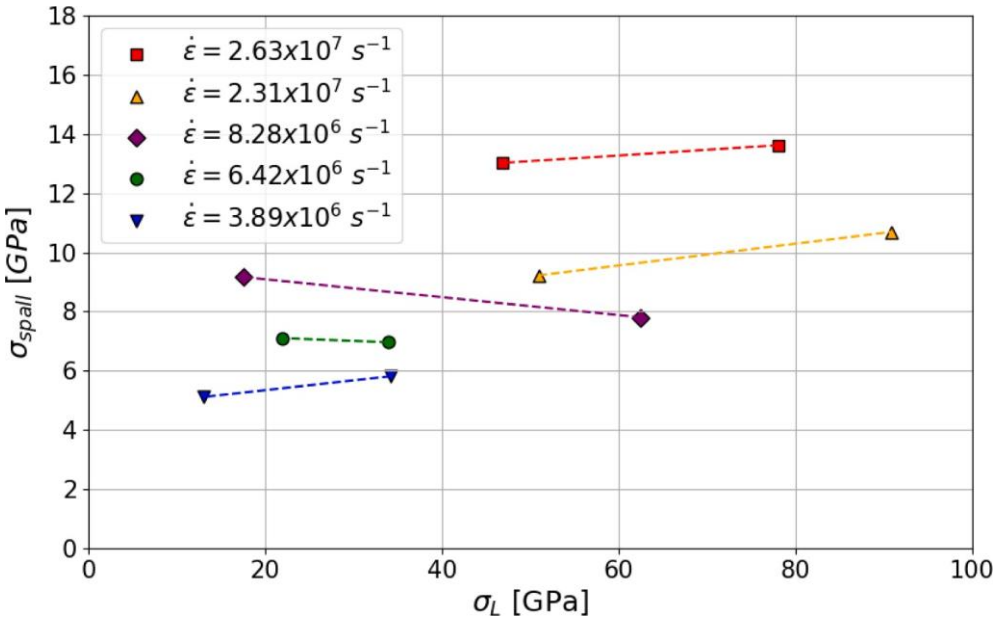

Fig. 9. Spall strength as a function of longitudinal stress for different values of strain rates.

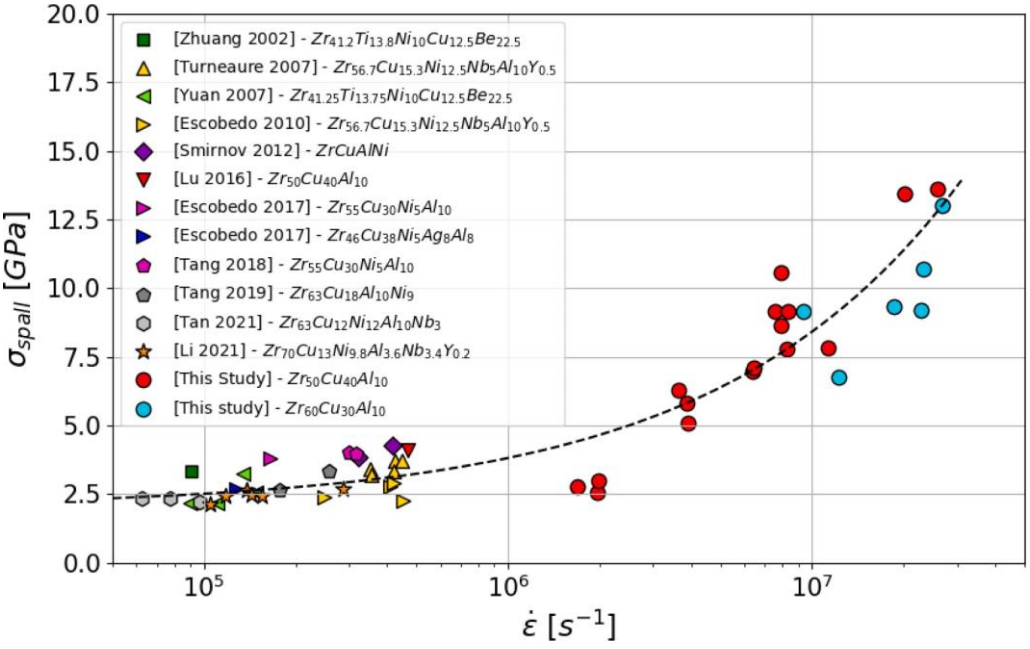

Fig. 10. Spall strength evolution with the strain rate. Comparison of results from this work compared with literature on Zr-based metallic glasses. Data from literature have been corrected using the method detailed in 2.2.

$$\sigma_R\ [GPa] = 3 \times 10^{-3}\ \dot{\varepsilon}^{0.386} + 0.74$$

$$\sigma_R\ [GPa] = 3 \times 10^{-4}\ \dot{\varepsilon}^{0.56} + 1.27$$

For aluminum and copper respectively.

One can notice that at a fixed strain rate value, our ternary compositions present an higher spall strength than aluminum and copper. According to these observations, one may suggest that bulk metallic glasses may require more energy to reach its damage threshold upon impact. Consequently, the mitigation capacity of bulk metallic glasses may be superior to aluminum as regards submilimeter space debris. This results are at some point consistent with [2,4,5],.

We finally focus on the results of this present work on $Zr_{50}Cu_{40}Al_{10}$ and $Zr_{60}Cu_{30}Al_{10}$ metallic glass compositions plotted on Fig. 12 with, this time, a linear x-axis for further analysis. This time we consider each composition apart. Here again, we fit the experimental data of each composition with a similar relationship than (9), considering the constant as the quasi-static tensile strength, which leads to the relations:

$$\sigma_R = 2.06 \times 10^{-4}\ \dot{\varepsilon}^{0.645} + 2$$

$$\sigma_R = 2.01 \times 10^{-5}\ \dot{\varepsilon}^{0.765} + 2$$

For for $Zr_{50}Cu_{40}Al_{10}$ and for $Zr_{60}Cu_{30}Al_{10}$

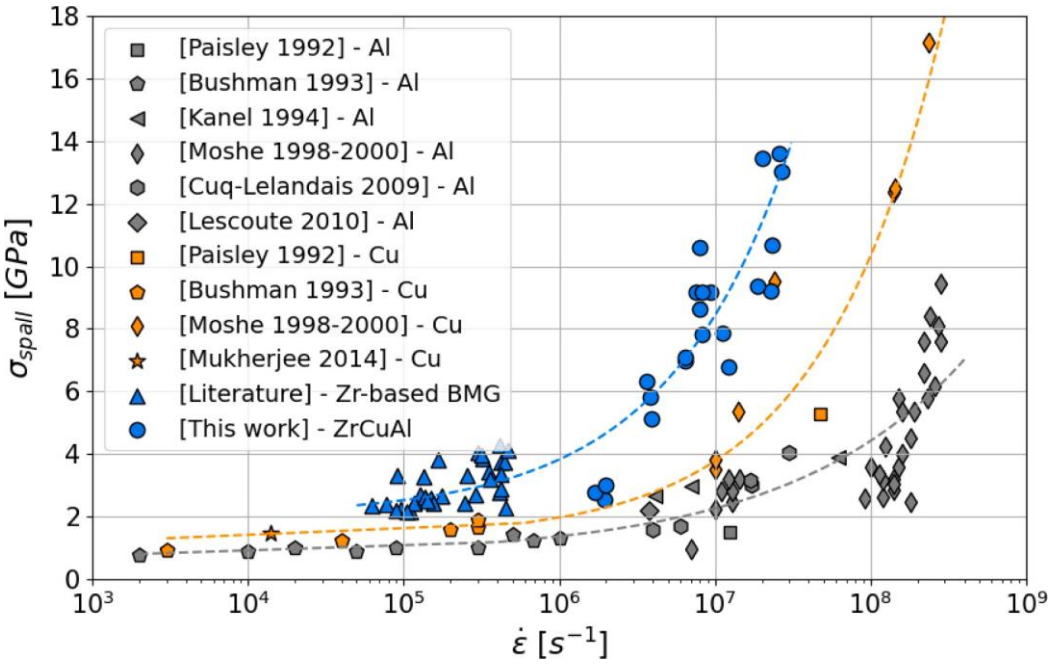

Fig. 11. Spall strength evolution with the strain rate. Comparison of all results on Zr-based metallic glasses (literature and this present work) with aluminum and copper.

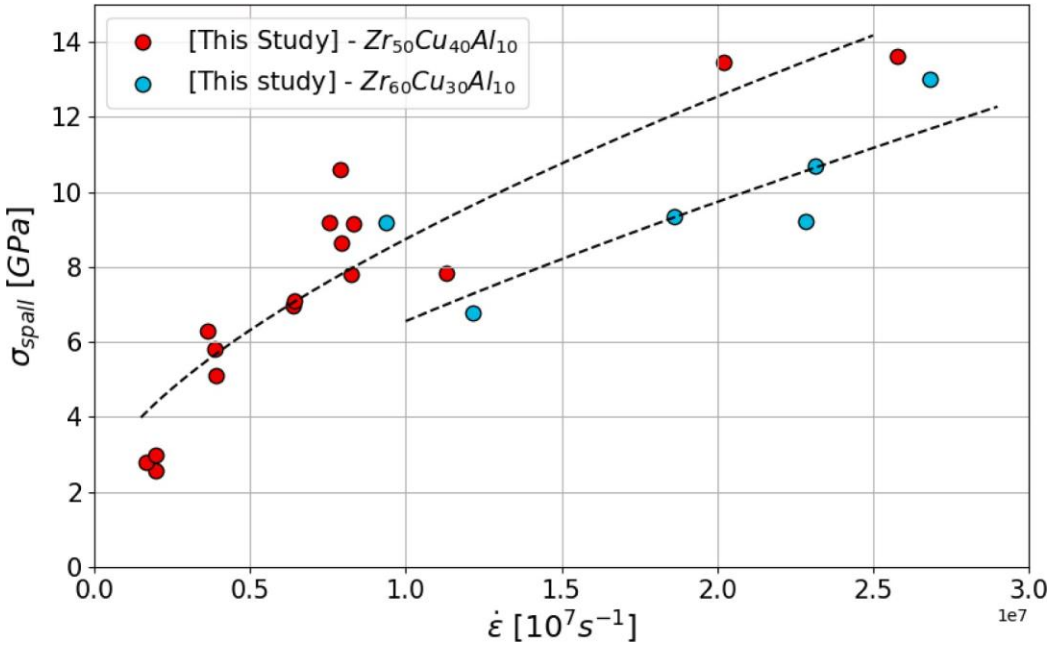

Fig. 12. Spall strength evolution with the strain rate of $Zr_{50}Cu_{40}Al_{10}$ and $Zr_{60}Cu_{30}Al_{10}$ metallic glasses with a linear x-axis.

Firstly, one may notice that for a given strain rate, $Zr_{60}Cu_{30}Al_{10}$ composition exhibit a lower spall strength than $Zr_{50}Cu_{40}Al_{10}$ composition. Differences in the spalling process of ZrCuAl bulk metallic glasses (including both compositions studied in this paper) has already been reported by Jodar *et al.* [41]. Secondly, the spall strength seems to converge towards a maximum limit value around 15 GPa for $Zr_{50}Cu_{40}Al_{10}$. This maximum limit value could also be called the ultimate theoretical strength and seems to be reached for strain rates higher than 2×10^7 s^{-1}. As already discussed by Kanel *et al.* [42] and Moshe *et al.*, [30] on previous works, the more the strain rate increases, the closer to the ultimate theoretical strength it gets. Indeed, by increasing the strain rate, the higher tensile region is getting thinner inside the sample. If we consider a finite number of potential initiation sites for fracture scattered in the sample thickness in a homogenous way, a thinner tensile region reduces the risk to engender an early fracture of a sample since the number of potential initiation sites is lower. Complementary laser driven-shock experiments with a shorter pulse duration are necessary to get more data at strain rates higher than 2.5×10^7 s^{-1} to confirm this behaviour. A load duration of approximately 5 ns on thinner samples to avoid the hydrodynamic damping should allow us to get such data.

4. Conclusion

This work brings new results on Zr-based metallic glasses obtained with laser shock experiments and complete the database started with plate impact experiments on the Hugoniot curves and on the evolution of the spall strength with the strain rate.

- We established for the first time the Hugoniot curve of $Zr_{50}Cu_{40}Al_{10}$ and $Zr_{60}Cu_{30}Al_{10}$ metallic glasses. The large amount of data show the robustness of the results with the comparisons between compositions and between the synthetization processes. Even though laser shock experiments lead to more dispersion, it is strongly consistent with literature up to 75 GPa. Divergence of the Hugoniot curves starting at 75 GPa still needs to be investigated with high pressure experiments (above 100 GPa) to validate a possible change of state observed on streak images and in molecular dynamic simulations.
- As for the evolution of the spall strength with the strain rate, we bring data in a new range of strain rate values, much higher than in previous works with plate impact experiments. These new data exhibit an increase of the spall strength with the strain rate of our ternary ZrCuAl metallic glasses. So far, this tendency was not so obvious and considered as quasi-constant comparing to the tensile strength in quasi-static domain. We have seen that such an evolution of the spall strength with the strain rate has already been reported in literature on common materials such as aluminum and copper. We have also demonstrated the importance of bringing new data in this strain rate range values for hypervelocity impact applications. Finally, we highlight once again differences in the spalling process of $Zr_{50}Cu_{40}Al_{10}$ and $Zr_{60}Cu_{30}Al_{10}$, and observed a tendency of the spall strength to converge towards the intrinsic strength of these metallic glass compositions around 15 GPa.

CRediT authorship contribution statement

Yoann Raffray: Formal analysis, Investigation, Data curation, Writing – original draft. **Benjamin Jodar:** Formal analysis, Investigation, Writing – original draft. **Jean-Christophe Sangleboeuf:** Conceptualization, Funding acquisition. **Alessandra Benuzzi-Mounaix:** Investigation, Validation. **Tommaso Vinci:** Software, Investigation. **Laurent Berthe:** Investigation, Validation. **Emilien Lescoute:** Investigation. **Etienne Barraud:** Investigation. **Erik Brambrink:** Investigation. **Rémi Daudin:** . **Jean-Jacques Blandin:** . **Didier Loison:** Methodology, Validation, Investigation, Writing – review & editing, Supervision, Project administration.

Declaration of Competing Interest

The authors declare the following financial interests/personal relationships which may be considered as potential competing interests:

Jean-Christophe Sangleboeuf reports financial support was provided by Brittany Region. Jean-Christophe Sangleboeuf reports financial support was provided by General Directorate of Armaments.

Data availability

Data will be made available on request.

Acknowledgments

The authors want to thank all the LULI members for their contribution during the experimental campaigns on nano2000 and HERA facilities, the CEA/DIF for providing an access to the GCLT facility and François Cheviré and Ronan Lebullenger for their help and expertise on DRX and DSC measurements. This work was supported by University of Rennes, DGA and ARED grants.

References

[1] Zheng W, Huang YJ, Pang BJ, Shen J. Hypervelocity impact on Zr51Ti5Ni10Cu25Al9 bulk metallic glass. Mater Sci Eng A 2011;529:352–60. https://doi.org/10.1016/j.msea.2011.09.043.
[2] Huang X, Ling Z, Liu ZD, Zhang HS, Dai LH. Amorphous alloy reinforced Whipple shield structure. Int J Impact Eng 2012;42:1–10. https://doi.org/10.1016/j.ijimpeng.2011.11.001.
[3] Davidson M, Roberts S, Castro G, Dillon RP, Kunz A, Kozachkov H, et al. Investigating amorphous metal composite architectures as spacecraft shielding. Adv Eng Mater 2013;15:27–33. https://doi.org/10.1002/adem.201200313.
[4] Hamill L, Roberts S, Davidson M, Johnson WL, Nutt S, Hofmann DC. Hypervelocity impact phenomenon in bulk metallic glasses and composites**: hypervelocity impact phenomenon in bulk metallic glasses and composites. Adv Eng Mater 2014;16:85–93. https://doi.org/10.1002/adem.201300252.
[5] Hofmann DC, Hamill L, Christiansen E, Nutt S. Hypervelocity impact testing of a metallic glass-stuffed whipple shield: hypervelocity impact testing of a metallic glass-stuffed.... Adv Eng Mater 2015;17:1313–22. https://doi.org/10.1002/adem.201400518.
[6] Li Y, Zhao S, Liu Y, Gong P, Schroers J. How many bulk metallic glasses are there? ACS Comb Sci 2017;19:687–93. https://doi.org/10.1021/acscombsci.7b00048.
[7] Martin M, Sekine T, Kobayashi T, Kecskes L, Thadhani NN. High-pressure equation of the state of a zirconium-based bulk metallic glass. Metall and Mat Trans A 2007;38:2689–96. https://doi.org/10.1007/s11661-007-9263-x.
[8] Mashimo T, Togo H, Zhang Y, Uemura Y, Kinoshita T, Kodama M, et al. Hugoniot-compression curve of Zr-based bulk metallic glass. Appl Phys Lett 2006;89:241904. https://doi.org/10.1063/1.2403931.
[9] Xi F, Yu Y, Dai C, Zhang Y, Cai L. Shock compression response of a Zr-based bulk metallic glass up to 110 GPa. J Appl Phys 2010;108:083537. https://doi.org/10.1063/1.3501044.
[10] Smirnov I., Atroshenko S., Sudenkov Y., Morozov N., Zheng W., Naumova N., et al. Dynamic properties of bulk metallic glass on the base of Zr, Chicago, Illinois: 2012, p. 1121–4. https://doi.org/10.1063/1.3686476.
[11] Li Y, Cheng X, Ma Z, Li X, Wang M. Dynamic response and damage evolution of Zr-based bulk metallic glass under shock loading. J Mater Sci Technol 2021;93: 119–27. https://doi.org/10.1016/j.jmst.2021.03.052.
[12] Zhuang S, Lu J, Ravichandran G. Shock wave response of a zirconium-based bulk metallic glass and its composite. Appl Phys Lett 2002;80:4522–4. https://doi.org/10.1063/1.1485300.
[13] Turneaure SJ, Dwivedi SK, Gupta YM. Shock-wave induced tension and spall in a zirconium-based bulk amorphous alloy. J Appl Phys 2007;101:043514. https://doi.org/10.1063/1.2537982.
[14] Yuan F, Prakash V, Lewandowski JJ. Spall strength and Hugoniot elastic limit of a zirconium-based bulk metallic glass under planar shock compression. J Mater Res 2007;22:402–11. https://doi.org/10.1557/jmr.2007.0053.
[15] Escobedo JP, Gupta YM. Dynamic tensile response of Zr-based bulk amorphous alloys: fracture morphologies and mechanisms. J Appl Phys 2010;107:123502. https://doi.org/10.1063/1.3447751.
[16] Lu L, Li C, Wang WH, Zhu MH, Gong XL, Luo SN. Ductile fracture of bulk metallic glass Zr 50 Cu 40 Al 10 under high strain-rate loading. Mater Sci Eng A 2016;651:848–53. https://doi.org/10.1016/j.msea.2015.11.040.
[17] Escobedo J.P., Chapman D.J., Laws K.J., Brown A.D., Wang F., Eakins D., et al. Effects of chemical composition on the shock response of zr-based metallic glasses, Tampa Bay, Florida, USA: 2017, p. 100032. https://doi.org/10.1063/1.4971657.
[18] Tang XC, Jian WR, Huang JY, Zhao F, Li C, Xiao XH, et al. Spall damage of a Ta particle-reinforced metallic glass matriX composite under high strain rate loading. Mater Sci Eng A 2018;711:284–92. https://doi.org/10.1016/j.msea.2017.11.032.
[19] Tang XC, Li C, Li HY, Xiao XH, Lu L, Yao XH, et al. Cup-cone structure in spallation of bulk metallic glasses. Acta Materialia 2019;178:219–27. https://doi.org/10.1016/j.actamat.2019.08.006.
[20] Tan Y, Wang YW, Cheng HW, Cheng XW. Dynamic fracture behavior of Zr63Cu12Ni12Al10Nb3 metallic glass under high strain-rate loading. J Alloys Comp 2021;853:157110. https://doi.org/10.1016/j.jallcom.2020.157110.
[21] Yokoyama Y, Fukaura K, Inoue A. Formation and mechanical properties of Zr-Cu-Al bulk glassy alloys. Mater Sci Eng A 2004;375–377:427–31. https://doi.org/10.1016/j.msea.2003.10.268.
[22] Yokoyama Y, Yamasaki T, Liaw PK, Buchanan RA, Inoue A. Glass-structure changes in tilt-cast Zr–Cu–Al glassy alloys. Mater Sci Eng A 2007;449–451:621–6. https://doi.org/10.1016/j.msea.2006.02.422.
[23] Chang JC, Nadeau F, Rosen M, Mehrabian R. Crystallization kinetics study of amorphous $Zr_{50}Cu_{50}$ by ultrasonic and micro hardness measurements. Scripta Metallurgica 1982;16:1073–8.
[24] Barker LM, Hollenbach RE. Laser interferometer for measuring high velocities of any reflecting surface. J Appl Phys 1972;43:4669–75. https://doi.org/10.1063/1.1660986.
[25] Celliers PM, Bradley DK, Collins GW, Hicks DG, Boehly TR, Armstrong WJ. Line-imaging velocimeter for shock diagnostics at the OMEGA laser facility. Rev Scient Instrum 2004;75:4916–29. https://doi.org/10.1063/1.1807008.
[26] GitHub NeutrinoToolkit/Neutrino. image analysis for plasma physics. https://github.com/NeutrinoToolkit/Neutrino. website accessible in 2023.
[27] Meyers MA. Dynamic behavior of materials. New York: Wiley; 1994.
[28] editor. In: Antoun T, editor. Spall fracture. New York: Springer; 2003.
[29] Moshe E, Eliezer S, Dekel E, Ludmirsky A, Henis Z, Werdiger M, et al. An increase of the spall strength in aluminum, copper, and Metglas at strain rates larger than 107 s—1. J Appl Phys 1998;83:4004–11. https://doi.org/10.1063/1.367222.

[30] Moshe E, Eliezer S, Henis Z, Werdiger M, Dekel E, Horovitz Y, et al. EXperimental measurements of the strength of metals approaching the theoretical limit predicted by the equation of state. Appl Phys Lett 2000;76:1555–7. https://doi.org/10.1063/1.126094.
[31] Cuq-Lelandais JP, Boustie M, Berthe L, de Rességuier T, Combis P, Colombier JP, et al. Spallation generated by femtosecond laser driven shocks in thin metallic targets. J Phys D Appl Phys 2009;42:065402. https://doi.org/10.1088/0022-3727/42/6/065402.
[32] Cuq-Lelandais JP. Study of spallation by sub-picosecond laser driven shocks in metals. EPJ Web Confer 2011:6.
[33] Lescoute E, De Rességuier T, Chevalier JM, Loison D, Cuq-Lelandais JP, Boustie M, et al. Ejection of spalled layers from laser shock-loaded metals. J Appl Phys 2010;108:093510. https://doi.org/10.1063/1.3500317.
[34] Mukherjee D, Rav A, Sur A, Joshi KD, Gupta SC. Shock induced spall fracture in polycrystalline copper. Patiala, Punjab, India: Thapar University; 2014. p. 608–10. https://doi.org/10.1063/1.4872691.
[35] Paisley D.L., Warnes R.H., Kopp R.A. Laser-driven flat plate impacts to 100 GPA with sub-nanosecond pulse duration and resolution for material property studies. Shock Compression of Condensed Matter–1991 1992:825–8. https://doi.org/10.1016/B978-0-444-89732-9.50189-8.
[36] Wen P, Demaske B, Spearot DE, Phillpot SR. Shock compression of Cu x Zr100_x metallic glasses from molecular dynamics simulations. J Mater Sci 2018;53: 5719–32. https://doi.org/10.1007/s10853-017-1666-5.
[37] Demaske BJ, Phillpot SR, Spearot DE. Atomic-level deformation of $Cu_x Zr_{100-x}$ metallic glasses under shock loading. J Appl Phys 2018;123:215101. https://doi.org/10.1063/1.5025650.
[38] Li C, Li B, Huang JY, Ma HH, Zhu MH, Zhu J, et al. Spall damage of a mild carbon steel: effects of peak stress, strain rate and pulse duration. Mater Sci Eng A 2016;660:139–47. https://doi.org/10.1016/j.msea.2016.02.080.
[39] Cuq-Lelandais JP, Boustie M, Berthe L, De Rességuier T. Behaviour of metals at ultra-high strain rate by using femtosecond laser shockwaves. EPJ Web Confer 2012;26:04013. https://doi.org/10.1051/epjconf/20122604013.
[40] Kanel GI, Razorenov SV, Utkin AV, Baumung K, Karow HU, Licht V. Spallations near the ultimate strength of solids. AIP Confer Proc 1994;309:1043–6. https://doi.org/10.1063/1.46273.
[41] Jodar B., Loison D., Yokoyama Y., Lescoute E., Dereure C., Nivard M., et al. Effects of zrcual bulk metallic glasses poisson's ratios on spalling process induced by laser shock, St. Louis, MO, USA: 2018, p. 070018. https://doi.org/10.1063/1.5044827.
[42] Kanel GI, Razorenov SV, Utkin AV. Spall strength of molybdenum single crystals. J Appl Phys 1993;74:5.